ROYAL SOCIETY
OF CHEMISTRY

PAPER

MoO$_2$ nanobelts@nitrogen self-doped MoS$_2$ nanosheets as effective electrocatalysts for hydrogen evolution reaction†

Weijia Zhou,*[a] Dongman Hou,[b] Yuanhua Sang,[c] Shuhua Yao,[d] Jian Zhou,[d] Guoqiang Li,[b] Ligui Li,[a] Hong Liu[c] and Shaowei Chen*[ae]

Advanced materials for electrocatalytic water splitting are central to renewable energy research. In this study, MoO$_2$ nanobelts@nitrogen self-doped MoS$_2$ nanosheets are produced by nitridation and sulfuration treatments of MoO$_3$ nanobelts. The material structures are characterized by a variety of techniques including scanning electron microscopy, transmission electron microscopy, Raman scattering, X-ray photoelectron spectroscopy, and X-ray diffraction spectroscopy. It is found that because of nitrogen doping and the abundance of exposed active edges, the heterostructures exhibit high electronic conductivity, and more importantly, enhanced and stable electrocatalytic activity in hydrogen evolution reaction (HER), as manifested in electrochemical studies. The onset potential is found to be only −156 mV (*vs.* RHE), which is 105 mV more positive than that of pure MoS$_2$ under identical experimental conditions. The corresponding Tafel slope is estimated to be 47.5 mV dec^{-1}, even slightly less than that of commercial 10 wt% Pt/C (49.8 mV dec^{-1}), suggesting that the reaction dynamics is largely determined by the electrochemical desorption of hydrogen. This is accounted for by nitrogen doping that leads to an enhanced electronic conductivity of the heterostructures as well as a high density of spinning electron states around the N and Mo atoms in MoS$_2$ nanosheets that are the active sites for HER, as manifested in density functional theory studies of a N-doped MoS$_2$ monolayer.

Introduction

With the ever increasing demand of energy and environmental protection on the global scale, development of technologies for clean and sustainable energy has been attracting great attention. As an alternative and renewable energy source, hydrogen has been hailed as a promising candidate to ameliorate the climate change and environmental problems associated with the combustion of fossil fuels. Toward this end, one effective approach is the production of hydrogen by environmentally friendly (photo)electrochemical water-splitting.[1–3] In these

[a]New Energy Research Institute, College of Environment and Energy, South China University of Technology, Guangzhou Higher Education Mega Center, Guangzhou, Guangdong 510006, China. E-mail: eszhouwj@scut.edu.cn

[b]College of Materials Science and Engineering, South China University of Technology, Wushan Road, Tianhe District, Guangzhou, Guangdong 510006, China

[c]State Key Laboratory of Crystal Materials, Center of Bio & Micro/Nano Functional Materials, Shandong University, 27 Shandanan Road, Jinan, Shandong 250100, China

[d]National Laboratory of Solid State Microstructures and Department of Materials Science and Engineering, Nanjing University, Nanjing, Jiangsu 210093, China

[e]Department of Chemistry and Biochemistry, University of California, 1156 High Street, Santa Cruz, California 95064, USA. E-mail: shaowei@ucsc.edu

† Electronic supplementary information (ESI) available: XRD patterns, Raman spectra, TEM image, additional voltammetric data, and theoretical results of DOS. See DOI: 10.1039/c4ta01898b

studies, advanced catalysts for the electrochemical hydrogen evolution reaction (HER) are necessary to reduce overpotential and increase energy efficiency.[4–6] To date, the most effective HER electrocatalysts are the Pt-group metals, which are known to catalyze HER at a significant rate with almost no overpotential.[7–9] However, the high costs and scarcity of Pt severely limit its widespread applications in HER, and it remains a great challenge to develop highly active HER catalysts based on abundant materials with a low overpotential.[10–12]

Towards this end, it has been found that MoS$_2$-based materials are the most effective non-Pt electrocatalysts for hydrogen production at low overpotentials.[13–15] Since the report by Hinnemann *et al.*[13] that MoS$_2$ nanoparticles are active HER catalysts, the interest in using MoS$_2$ and related metal sulfides as water-splitting electrocatalysts has intensified.[16–18] Computational studies confirm that the HER activity stems largely from the molybdenum edges of MoS$_2$;[14] and the activity can be modified by nanostructure morphologies (*e.g.*, nanowires and nanosheets),[19,20] or by supporting substrates (*e.g.*, Si wires, graphene-protected 3D nickel foams, and graphene nanosheets).[21–23] For instance, Dai *et al.*[22] synthesized MoS$_2$ nanoparticles on reduced graphene nanosheets *via* a facile solvothermal procedure, which exhibited excellent HER activity with a small overpotential of ∼100 mV, large cathodic currents, and a Tafel slope as small as 41 mV dec^{-1}. They attributed the

good HER performance to the highly exposed edges of MoS_2 and excellent electronic coupling to the underlying graphene sheets. However, further enhancement of the exposure of active edge sites and improvement in electronic conductivity have remained great challenges for MoS_2-based HER electrocatalysts. This is the primary motivation of the present study.

Herein, deliberate doping with nitrogen was employed to enhance the HER activity of MoS_2 electrocatalysts. Doping treatments with non-metals (e.g., N, S, B, and P)[24-27] and metals (e.g., Fe and Zn)[28,29] have been used rather extensively to enhance the electrocatalytic activity in oxygen reduction reaction (ORR) and oxygen evolution reaction (OER). Yet, to our knowledge, there has been no report on the enhancement of the HER performance of MoS_2 nanosheets by doping with either metallic or nonmetallic elements. In the present study, MoO_2 nanobelts coated with nitrogen self-doped MoS_2 nanosheets were prepared via a hydrothermal reaction between thioacetamide and $MoO_2@Mo_2N$ nanobelts, and the structures were characterized by a variety of experimental techniques. Electrochemical studies showed that the obtained N-doped heterostructures exhibited a remarkable electrocatalytic activity for HER, where the onset potential (-156 mV vs. RHE) was markedly more positive than those of MoS_2, Mo_2N, and MoO_3. This was accounted for by the nitrogen doping that led to the enhanced electronic conductivity of the heterostructures as well as a high density of spinning electron states around the N and Mo atoms in MoS_2 nanosheets that were the active sites for HER, as manifested in density functional theory studies of a N-doped MoS_2 monolayer.

Experimental section

Materials

All reagents were of analytical grade and used without further purification. Molybdenum powders (Mo), hydrogen peroxide (H_2O_2), cyanamide ($C_2H_4N_4$), thioacetamide (C_2H_5NS, TAA), and 10 wt% Pt/C were obtained from Sinopharm Chemical Reagents Beijing Co. Water was supplied by a Barnstead Nanopure Water System (18.3 MΩ cm).

Synthesis of MoO_3 nanobelts

MoO_3 nanobelts were synthesized by a simple hydrothermal procedure.[30] In a typical reaction, 0.1 g of Mo metal powders was slowly added to 16 mL of 35% H_2O_2 under vigorous stirring in an ice-water bath, forming a yellow solution of the precursor compound $MoO_2(OH)(OOH)$, which was then loaded into a 20 mL Teflon-lined autoclave and heated at 200 °C for 24 h. After cooling to room temperature, the white precipitates were then centrifuged and washed with deionized water several times. After drying in vacuum at 70 °C for 12 h, MoO_3 nanobelts were collected as white powders.

Synthesis of $MoO_2@Mo_2N$ nanobelts

In a typical experiment, 50 mg of the MoO_3 nanobelts prepared above was dispersed into 50 mL of ethanol with 20 mg of cyanamide under continuous stirring. The products were heated at 450 °C for 1 h, then 650 °C for 2 h under an argon atmosphere to convert the single-crystalline MoO_3 nanobelts into porous MoO_2 core@Mo_2N shell nanobelts.

Synthesis of MoO_2 nanobelts@nitrogen self-doped MoS_2 nanosheets

MoO_2 nanobelts@nitrogen self-doped MoS_2 nanosheets were synthesized as follows. In a typical reaction, 20 mg of the $MoO_2@Mo_2N$ nanobelts obtained above and 80 mg of thioacetamide (C_2H_5NS) were dissolved in 20 mL of deionized water. The solution was transferred to a Teflon-lined stainless steel autoclave and then heated in an electric oven at 200 °C for 24 h. The black product, $MoO_2@$N-doped MoS_2, was harvested after centrifugation and dried at 70 °C for 12 h. For comparison, powders of pure MoS_2 nanosheets were synthesized under the same conditions by using MoO_3 nanobelts instead of $MoO_2@Mo_2N$ nanobelts as the precursors.

Characterization

Field-emission scanning electron microscopic (FESEM, Model JSM-7600F) measurements were used to characterize the morphologies of the samples. Transmission electron microscopic (TEM) measurements were carried out with a JOEL JEM 2100F microscope. Powder X-ray diffraction (XRD) patterns of the samples were recorded on a Bruker D8 Advance powder X-ray diffractometer with Cu Kα ($\lambda = 0.15406$ nm) radiation. X-ray photoelectron spectroscopic (XPS) measurements were performed using an ESCALAB 250 instrument. Raman spectra were recorded on a RENISHAW inVia instrument with an Ar laser source of 488 nm in a macroscopic configuration.

Electrochemistry

Electrochemical measurements were performed with an electrochemical workstation (CHI 760C, CH Instruments Inc.) in a 0.5 M H_2SO_4 aqueous solution. A Ag/AgCl electrode (saturated KCl) and platinum wire were used as the reference and counter electrode, respectively. 4 mg of the catalyst powders was dispersed in 1 mL of 4 : 1 (v/v) water–ethanol mixed solvent along with 80 μL of Nafion solution, and the mixture was ultrasonicated for 30 min. Then, 5 μL of the solution prepared above was dropcast onto the surface of a glassy carbon (GC) disk electrode at a catalyst loading of 0.285 mg cm^{-2}. The as-prepared catalyst film was dried at room temperature. The polarization curves were obtained by sweeping the potential from 0 to -0.8 V (vs. Ag/AgCl) at a potential sweep rate of 5 mV s^{-1}. The accelerated stability tests were performed in 0.5 M H_2SO_4 at room temperature by potential cycling between 0 and -0.6 V (vs. Ag/AgCl) at a sweep rate of 100 mV s^{-1} for a given number of cycles. Current–time responses were monitored by chronoamperometric measurements for 12 h.

In all measurements, the Ag/AgCl reference electrode was calibrated with respect to a reversible hydrogen electrode (RHE). The calibration was performed in a high-purity H_2 (99.999%) saturated electrolyte with a Pt wire as the working electrode and counter electrode. Cyclic voltammograms (CVs) were collected at a scan rate of 1 mV s^{-1}, and the average of the two potentials

at which the current crossed zero was taken as the thermodynamic potential for the hydrogen electrode reactions. In 0.5 M H_2SO_4, $E(Ag/AgCl) = E(RHE) + 0.246$ V (Fig. S1†).

Theoretical calculations

The geometric and electronic properties of N-doped MoS_2 were calculated by density functional theory studies in the generalized gradient approximation implemented in the Vienna *Ab initio* Simulation Package (VASP),[31,32] in which the projected augmented wave method[33,34] and Perdew–Burke–Ernzerhof exchange correlation[35] were used. The plane-wave cutoff energy was 520 eV throughout the calculations. The Brillouin zone integrations were performed with a $(3 \times 3 \times 1)$ Γ-center k-point mesh and the Gaussian smearing width was 0.05 eV. In order to simulate the N-doped MoS_2, we constructed a (4×4) supercell based on the primitive cell of a MoS_2 monolayer, in which an S atom is replaced by an N atom. Then the atomic positions were relaxed by using the conjugate-gradient algorithm until the residual forces of all atoms were less than 0.02 eV $Å^{-1}$.

Results and discussion

Fig. 1 describes the procedure for a typical synthesis of MoO_2@N-doped MoS_2 nanobelts, which involves three major steps: (a) the surface of MoO_3 nanobelts was coated with a thin film of cyanamide; (b) the cyanamide/MoO_3 nanobelts were calcined at 650 °C under an argon atmosphere to obtain MoO_2@Mo_2N nanobelts by the decomposition of the cyanamide polymer; and (c) the resulting products were hydrothermally treated with thioacetamide (TAA) to produce nitrogen-doping MoS_2 nanosheets on MoO_2 nanobelts. The morphologies of the as-prepared MoO_2 nanobelts@nitrogen-doped MoS_2 nanosheets were firstly examined by using field-emission scanning electron microscopic (FE-SEM) measurements. Fig. 2a presents an overview of the smooth MoO_3 nanobelts which are 80–400 nm in width and 5–10 μm in length. After calcination at 650 °C under an argon atmosphere, porous nanobelts composed of MoO_2 and Mo_2N were obtained (Fig. 2b), which was confirmed by XRD measurements (Fig. S2†). The obtained porous MoO_2@Mo_2N nanobelts were then used as Mo and N sources to synthesize N-doped MoS_2. From Fig. 2c and d, it can

Fig. 2 Representative SEM images of (a) MoO_3 nanobelts, (b) MoO_2@Mo_2N nanobelts, and (c and d) MoO_2 nanobelts@nitrogen-doped MoS_2 nanosheets.

be seen that after hydrothermal treatment with TAA, the nanobelts surfaces were homogeneously decorated with a number of curvy nanosheets. XRD studies show that the diffraction peaks of Mo_2N disappeared and the remaining diffraction features were primarily due to MoO_2 (Fig. S2†). While no diffraction peaks were identified for MoS_2 in XRD measurements (Fig. S2†), Raman spectroscopic studies (Fig. S3†) did show that MoS_2 was formed with a characteristic vibrational band at 377.8 cm^{-1}. This suggests that the nanosheets observed in Fig. 2d was most likely composed of MoS_2, leading to the formation of a MoO_2@N-doped MoS_2 core–shell heterostructure.

XPS measurements were then carried out to further investigate the chemical composition and valence states of the samples, which were depicted in Fig. 3 and summarized in Table 1. From the survey spectra in panel (a), the element of Mo can be clearly identified in all samples, with S found only in MoO_2@N-doped MoS_2 (curve 3). Fig. 3b depicts the high-resolution scans of the Mo3d electrons, where one can see two peaks at 236.2 eV and 233.2 eV in the starting MoO_3 nanobelts (curve 1), consistent with $Mo3d_{3/2}$ and $3d_{5/2}$ of Mo^{6+}. After calcination reactions of MoO_3 nanobelts and cyanamide (curve 2), both Mo^{4+} (located at 229.5 and 232.5 eV, blue and aqua-blue peaks) and Mo^{2+} (located at 231.5 eV, magenta peak) can be identified, as a result of the formation of MoO_2 and Mo_2N,[36] respectively, which is consistent with the XRD results in Fig. S2b.† After the hydrothermal reaction with TAA (curve 3), only Mo^{4+} was observed (blue and aqua-blue peaks), but with different covalent bonds of MoS_2 (227.2 eV) and MoO_2 (232.7 and 229.5 eV). Meanwhile, the S2p electrons exhibited various bonding energies for S^{2-} (162.2 eV, 163.2 eV, 164.1 eV, 165.1 eV) and S^{6+} (168.5 eV) (curve 3 in panel c). This is likely due to the different
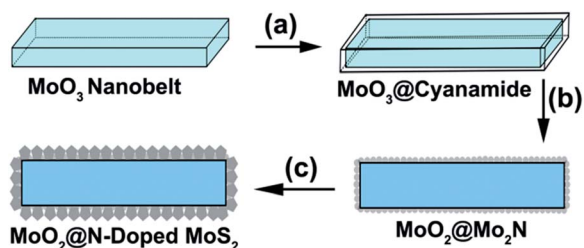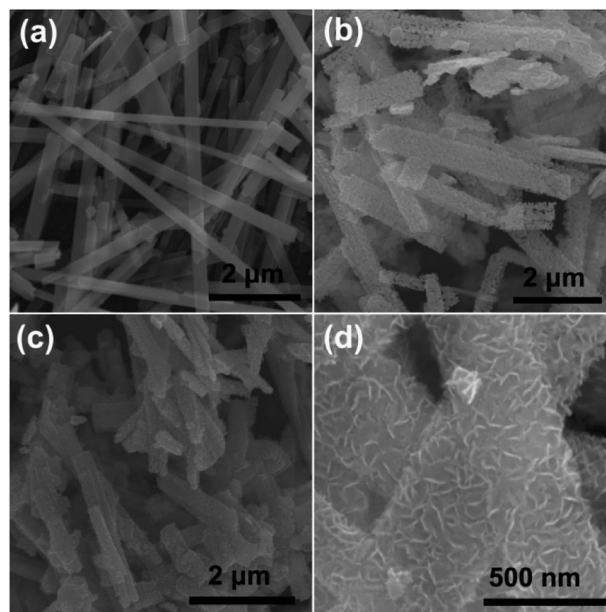

Fig. 1 Schematic of the synthesis of MoO_2@N-doped MoS_2 nanobelts: (a) MoO_3 nanobelts mixed with a cyanamide ethanol solution, (b) transformation into MoO_2@Mo_2N nanobelts by calcination at 650 °C for 2 h, and (c) hydrothermal reactions of MoO_2@Mo_2N nanobelts with TAA.

11360 | *J. Mater. Chem. A*, 2014, **2**, 11358–11364

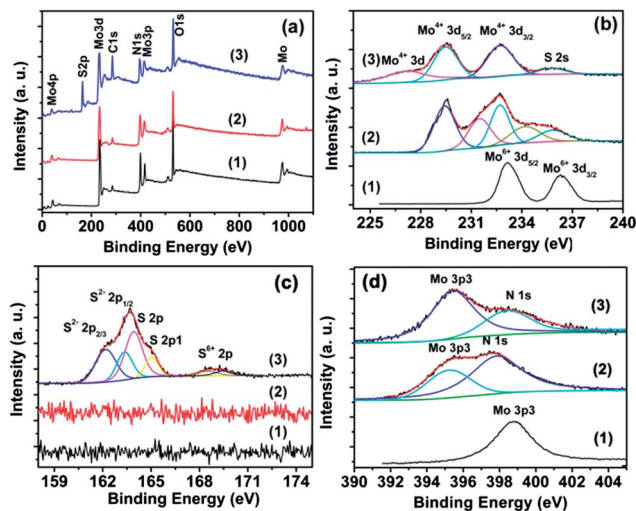This journal is © The Royal Society of Chemistry 2014

Fig. 3 (a) XPS survey spectra and high-resolution scans of (b) Mo3d, (c) S2p and (d) N1s electrons of (1) MoO_3 nanobelts, (2) MoO_2@Mo_2N nanobelts and (3) MoO_2@N-doped MoS_2 heterostructures.

Fig. 4 TEM images of (a and b) MoO_3 nanobelts, (c and d) MoO_2@Mo_2N nanobelts and (e and f) MoO_2 nanobelts@nitrogen self-doped MoS_2 nanosheets, and (g) EDS elemental maps for a MoO_2@N-doped MoS_2 heterostructure.

environments of S caused by nitrogen-doping in MoS_2.[37] Note that the S signals were totally absent in the MoO_3 and MoO_2@Mo_2N nanobelts (curves 1 and 2 in Fig. 3c). The formation of N-doped MoS_2 nanosheets was further manifested in the measurements of the N1s electrons as depicted in Fig. 3d. For MoO_2@Mo_2N (curve 2), the $Mo3p_{3/2}$ and N1s electrons can be identified at 395.5 eV (aqua-blue peak) and 397.5 eV (blue peak), respectively, consistent with the formation of Mo–N bonding linkages;[38] and after hydrothermal treatments, the N1s peak in curve (3) was found to blue-shift to 398.5 eV, likely because of the formation of MoS_2 nanosheets where Mo carried a higher oxidation state and N was embedded into the nanosheet matrix (Fig. 1). Similar self-doping reactions have also been carried out to synthesize N-doped TiO_2 from TiN_2.[39,40] One may notice that there is a substantial overlap between the $Mo3p_{3/2}$ and N1s electrons, which renders it difficult to have an accurate quantitative analysis of the elements.

Fig. 4 show the representative TEM images of the resulting MoO_3 nanobelts, MoO_2@Mo_2N nanobelts and MoO_2 nanobelts@N-doped MoS_2 nanosheets. The smooth nanobelt morphology for MoO_3 and porous nanobelt morphology for MoO_2@Mo_2N can be clearly seen in Fig. 4a and c, respectively, consistent with the SEM results in Fig. 2; and for the MoO_2 nanobelts@N-doped MoS_2 nanosheets, it can be seen that the
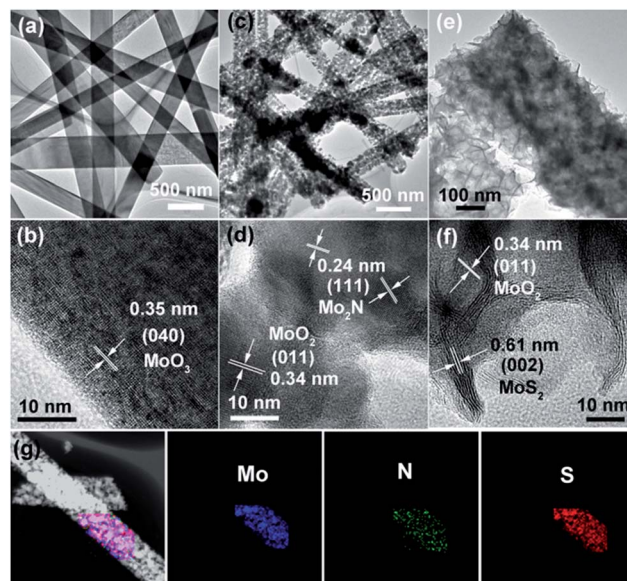
MoO_2 nanobelts were uniformly decorated with MoS_2 nanosheets (Fig. 4e). Most of the MoS_2 nanosheets were aligned perpendicular to the surface of the nanobelts, which have been known to possess abundant folded edges with high catalytic activity for HER.[6] From Fig. 4f, the (002) planes of MoS_2 can be clearly seen with a lattice spacing of 0.61 nm; and from the HRTEM images in Fig. 4b, d and f, the periodic fringe spacings of 0.35 nm, 0.34 nm, and 0.24 nm agree well with the interplanar spacings of (040) for MoO_3 (orthorhombic, $a = 0.40$ nm, $b = 1.38$ nm, $c = 0.37$ nm), (011) for MoO_2 (monoclinic, $a = 0.56$ nm, $b = 0.48$ nm, $c = 0.55$ nm), and (111) for Mo_2N (cubic, $a = b = c = 0.416$ nm), respectively. Furthermore, elemental mapping based on energy dispersive X-ray (EDS) analysis clearly shows that the MoO_2@N-doped MoS_2 consists of Mo, N, and S elements (Fig. 4g), and the N element was distributed evenly in the heterostructured nanobelt. This again confirmed that the N element was indeed doped into the MoS_2 nanosheets.

The electrocatalytic activities for HER of the nanobelts prepared above were then examined by electrochemical measurements in 0.5 M H_2SO_4. From Fig. 5a, it can be seen that the bare GC electrode exhibited almost no catalytic activity for

Table 1 Summary of elemental composition, binding energy, and valence state of different samples by XPS measurements

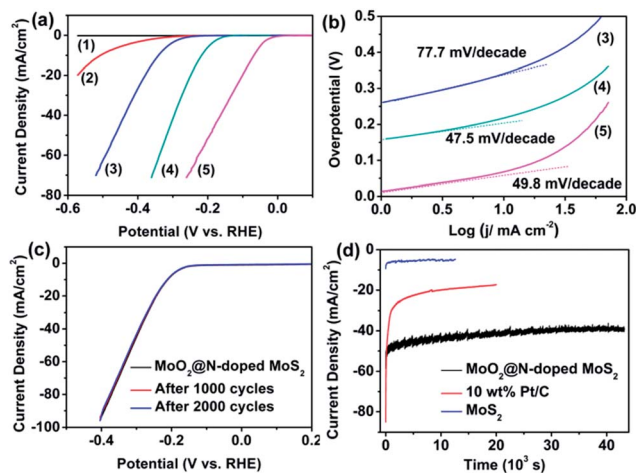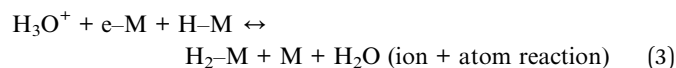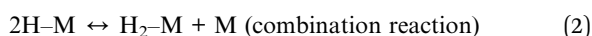| Samples	Elements	Binding energy (eV)	Valence state
MoO_3 nanobelts	Mo	389.5; 236.2, 233.2	+6
MoO_2@Mo_2N nanobelts	Mo	395.5; 232.5, 229.5, (Mo^{4+}) and 231.5 (Mo^{2+})	+2, +4
	N	397.5	−4
MoO_2@N-doped MoS_2	Mo	395.5; 232.7, 229.5, 227.2	+4
	N	398.5	0
	S	162.2, 163.2, 164.1, 165.1 (S^{2-}), and 168.5 eV (S^{6+})	−2, +6

Fig. 5 (a) Polarization curves for HER in 0.5 M H_2SO_4 on (1) a bare glassy-carbon (GC) electrode, and the GC electrode modified by (2) MoO_2@Mo_2N, (3) MoS_2, and (4) MoO_2@N-doped MoS_2, as well as (5) 10 wt% Pt/C. Potential sweep rate 5 mV s^{-1}. (b) Corresponding Tafel plots (overpotential *versus* log current) derived from (a). (c) HER polarization curves for MoO_2@N-doped MoS_2 before and after 2000 cycles in the stability test. Potential sweep rate 100 mV s^{-1}. (d) Current–time plots of the MoO_2@N-doped MoS_2 electrode at the applied potential of −0.25 V (*vs.* RHE) under the same conditions.

HsER (curve 1). In sharp contrast, apparent non-zero cathodic currents can be seen at the electrode modified by MoO_2@N-doped MoS_2 with an onset potential of −0.156 V (*vs.* RHE) (curve 4). This corresponds to an overpotential (η) of only −156 mV. Such a performance is markedly better than those of pure MoS_2 (η = −261 mV, curve 3) and MoO_2@Mo_2N (η = −334 mV, curve 2) at the same catalyst loading. Whereas one may notice that the activity remains subpar as compared to that of commercial 10 wt% Pt/C catalysts (η = −14 mV, curve 5), it is worth noting that the coverage of MoS_2 in MoO_2@N-doped MoS_2 was too low to be detected by XRD measurements (Fig. S2†). Yet, even at such a low content of MoS_2, the MoO_2@N-doped MoS_2 heterostructures possess the highest HER catalytic activity among the nanostructure series.

The enhanced performance in HER for MoO_2@N-doped MoS_2, as compared to that of MoS_2 alone, was further manifested in the corresponding Tafel plots. From Fig. 5b, one can see that at the same overpotentials, the current density at the MoO_2@N-doped MoS_2 electrode was at least an order of magnitude higher than that at MoS_2. Note that for hydrogen evolution in acid on metal electrode surfaces, the mechanism typically involves three major reactions,[41]

$$H_3O^+ + e–M \leftrightarrow H–M + H_2O \quad \text{(discharge reaction)} \quad (1)$$

$$2H–M \leftrightarrow H_2–M + M \quad \text{(combination reaction)} \quad (2)$$

$$H_3O^+ + e–M + H–M \leftrightarrow$$
$$H_2–M + M + H_2O \quad \text{(ion + atom reaction)} \quad (3)$$

where e–M denotes metal-bound electrons, while H–M and H_2–M represent a hydrogen atom and molecule adsorbed onto a

surface metal atom, respectively. Various Tafel slopes have been predicted and observed. For instance, a slope of 30 mV dec^{-1} has been found to correspond to a fast discharge reaction (1) followed by a rate-determining combination reaction (2); whereas a high slope of 40 mV dec^{-1} is proposed to signify a fast discharge reaction (1) followed by the ion + atom reaction (3), corresponding to a transfer coefficient (α) of ∼0.5. From Fig. 5b, linear regressions of the linear portions by the Tafel equation, $\eta = b \log j + a$, yield a slope of 49.8, 47.5, and 77.7 mV dec^{-1} for 10 wt% Pt/C (curve 5), MoO_2@N-doped MoS_2 (curve 4) and pure MoS_2 (curve 3), respectively. Note that in a previous study of HER with MoS_2 nanoparticles supported on graphene,[22] a Tafel slope of 41 mV dec^{-1} was observed, which suggested that the rate-determining step of HER was the electrochemical desorption of hydrogen. In the present study, the fact that the Tafel slopes for commercial Pt/C and MoO_2@N-doped MoS_2 were almost identical indicates that the reaction pathways for HER were likely similar on these two catalysts at rather comparable electron-transfer kinetics. This may account for the low overpotential (and hence enhanced performance) observed for MoO_2@N-doped MoS_2, with electrochemical desorption of hydrogen being the rate-determining step, in comparison to pure MoS_2.

In addition to good catalytic activity, the MoO_2@N-doped MoS_2 electrode also exhibited good stability for HER. Fig. 5c shows that, even after 2000 potential cycles, the j–V curve of the MoO_2@N-doped MoS_2 electrode remained almost unchanged. The reverse scans also confirmed the good HER stability of the MoO_2@N-doped MoS_2 electrode (Fig. S4†). To further investigate the stability of MoO_2@N-doped MoS_2 in HER, the current–time plots at the applied potential of −0.25 V (*vs.* RHE) was depicted in Fig. 5d. It can be seen that commercial Pt/C catalysts (red curve) exhibited a much higher initial current than MoS_2 (blue curve) and MoO_2@N-doped MoS_2 (black curve); yet the steady-state current of MoO_2@N-doped MoS_2 was the highest among the three. For instance, the current density of MoO_2@N-doped MoS_2 at 2 h is 8.1 times and 2.2 times higher than those of pure MoS_2 and 10 wt% Pt/C, respectively. Notably, the current remained steady over 12 h of continuous operation (black curve), indicating excellent durability of the MoO_2@N-doped MoS_2 electrode for HER in 0.5 M H_2SO_4.

It should be noted that while the overpotential and Tafel slope of MoO_2@N-doped MoS_2 in HER were somewhat higher than those reported previously,[22,42] the enhancement of the HER performance by the nitrogen-doping procedure above is markedly more pronounced than by other mechanisms. For instance, the overpotential for HER was reduced by 105 mV with MoO_2@N-doped MoS_2, as compared to that of pure (unsupported) MoS_2 (Fig. 5). In comparison, the overpotential was reduced by only about 60 mV with defect-rich MoS_2, relative to that of defect-free MoS_2;[42] and for MoS_2 nanoparticles supported on reduced graphene nanosheets, the overpotential was reduced by only 50 mV as compared to that of unsupported MoS_2 nanoparticles[22] (Table S1†). It should be noted that in the present study, the remarkable performance of MoO_2@N-doped MoS_2 in HER was observed despite a low content of MoS_2 (not detectable in XRD measurements, Fig. S2†). Thus, further work

11362 | *J. Mater. Chem. A*, 2014, 2, 11358–11364

This journal is © The Royal Society of Chemistry 2014

is required to examine the effects of nitrogen doping and MoS_2 loading on the electrocatalytic activity for HER.

The aforementioned enhancement of the HER performance of MoO_2@N-doped MoS_2 can be attributed to the following factors. The first is the high electronic conductivity of MoO_2@N-doped MoS_2. Indeed, electrochemical impedance spectroscopic measurements of MoS_2 and MoO_2@N-doped MoS_2 showed that the charge-transfer resistance of MoO_2@N-doped MoS_2 for HER is markedly smaller than that for the bare MoS_2 nanosheets (Fig. S5†). This low resistivity may also be facilitated by the aligned perpendicular growth of MoS_2 nanosheets on the MoO_2 nanobelt surface. MoS_2 with a sandwiched layer structure is composed of Mo atoms situated between two layers of hexagonally close-packed sulfur atoms, and the MoS_2 layers are stacked together by van der Waals interactions. In this configuration, the electronic conductivity parallel to the layered structure of the MoS_2 nanosheets is much higher than that along the vertical direction.[12] Therefore, the perpendicular growth of MoS_2 nanosheets on the conductive substrates is advantageous for electron transport between MoS_2 and MoO_2 nanobelts.[6] Second, N doping in MoS_2 nanosheets synthesized from Mo_2N most likely results in the exposure of additional active edge sites, as depicted in the schematic representation in Fig. S6.† The S atoms in MoS_2 are partially replaced by N atoms, leading to a high density of defects and exposure of Mo edges that are known for high HER activity. In fact, defect-rich MoS_2 nanosheets can be identified in HRTEM studies of MoO_2@N-doped MoS_2 (Fig. S7†). Notably, whereas controlled growth of MoS_2 nanomaterials with exposed Mo edges has been reported before,[14,42] to our knowledge this is the first ever report of nitrogen self-doping treatment of MoS_2 nanosheets to further enhance the HER activity.

The mechanistic interpretations above were also consistent with results from theoretical calculations. Fig. 6 and S8† depict the spin polarized density of states (DOS) and spin polarized charge density of a nitrogen-doped MoS_2 nanosheet. It can be clearly seen that there are two peaks near the Fermi energy (Fig. S8†). The spin-up peak is totally occupied, while the spin-down peak is totally vacant. This spin split in DOS leads to a 1.0 μ_B magnetic moment in the supercell. In Fig. 6, the spin polarized charge density indicates that the magnetic moment mostly arises from the N atoms and spreads to the nearby Mo

and S atoms. Therefore the doped N atoms likely provide a localized state near the Fermi energy in the band gap of the semiconducting MoS_2. That is, there is a high density of electronic states around the N and Mo atoms, which is consistent with the enhanced electronic conductivity of the MoO_2@N-doped MoS_2 heterostructures (Fig. S5†). Furthermore, such electron-rich sites are critical and beneficial for HER where the negative charge is anticipated to help attract and chemisorb H^+ to the catalyst surface, a critical first step in HER, ultimately leading to improved HER performance.

Conclusion

In this study, an effective electrocatalyst based on earth-abundant and inexpensive components was developed for hydrogen evolution reaction. MoO_2 nanobelts@nitrogen self-doped MoS_2 nanosheets were produced by nitridation and sulfuration treatments of MoO_3 nanobelts. The MoS_2 nanosheets were found to grow perpendicular on the MoO_2 nanobelt surface such that the heterostructures possessed high electronic conductivity and abundant exposed active edges. Electrochemical studies showed that the obtained electrocatalysts exhibited excellent HER activity with an onset potential of -156 mV (*vs.* RHE), a large current density, a small Tafel slope of 47.5 mV dec^{-1} and prominent electrochemical durability, in comparison with commercial Pt/C catalysts. DFT calculations suggested a high density of electronic states around the N and Mo atoms which was likely responsible for the enhanced electronic conductivity as well as apparent HER performance of the MoS_2 nanosheets. Such a strategy based on doping engineering of HER catalysts with N, P and B elements may pave the way towards the design and preparation of highly efficient catalysts for water splitting.

Acknowledgements

Notes and references

1 E. Anxolabéhère-Mallart, C. Costentin, M. Fournier, S. Nowak, M. Robert and J.-M. Savéant, *J. Am. Chem. Soc.*, 2012, **134**, 6104–6107.

2 R. Subbaraman, D. Tripkovic, D. Strmcnik, K.-C. Chang, M. Uchimura, A. P. Paulikas, V. Stamenkovic and N. M. Markovic, *Science*, 2011, **334**, 1256–1260.

3 C. C. L. McCrory, C. Uyeda and J. C. Peters, *J. Am. Chem. Soc.*, 2012, **134**, 3164–3170.

4 C. He, X. Wu, J. Shen and P. K. Chu, *Nano Lett.*, 2012, **12**, 1545–1548.

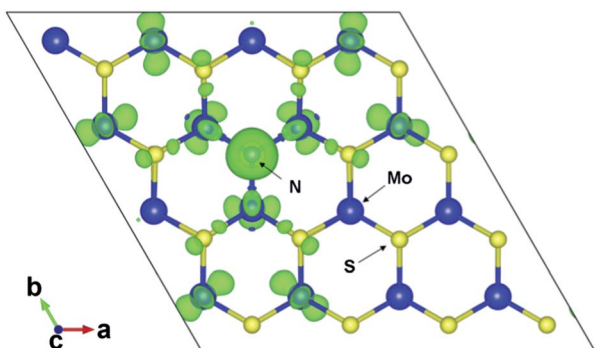5 M. L. Helm, M. P. Stewart, R. M. Bullock, M. R. DuBois and D. L. DuBois, *Science*, 2011, **333**, 863–866.

Fig. 6 Spin polarized charge density of a N-doped MoS_2 monolayer.

This journal is © The Royal Society of Chemistry 2014

J. Mater. Chem. A, 2014, **2**, 11358–11364 | **11363**

Journal of Materials Chemistry A   Paper

6 D. Kong, H. Wang, J. J. Cha, M. Pasta, K. J. Koski, J. Yao and Y. Cui, *Nano Lett.*, 2013, **13**, 1341–1347.

7 D. V. Esposito, S. T. Hunt, A. L. Stottlemyer, K. D. Dobson, B. E. McCandless, R. W. Birkmire and J. G. Chen, *Angew. Chem., Int. Ed.*, 2010, **122**, 10055–10058.

8 I. E. L. Stephens and I. Chorkendorff, *Angew. Chem., Int. Ed.*, 2011, **50**, 1476–1477.

9 J. Greeley, J. K. Nørskov, L. A. Kibler, A. M. El-Aziz and D. M. Kolb, *ChemPhysChem*, 2006, **7**, 1032–1035.

10 P. D. Tran, A. Le Goff, J. Heidkamp, B. Jousselme, N. Guillet, S. Palacin, H. Dau, M. Fontecave and V. Artero, *Angew. Chem., Int. Ed.*, 2011, **50**, 1371–1374.

11 L. He, Y. Huang, A. Wang, X. Wang, X. Chen, J. J. Delgado and T. Zhang, *Angew. Chem., Int. Ed.*, 2012, **51**, 6191–6194.

12 A. B. Laursen, S. Kegnaes, S. Dahl and I. Chorkendorff, *Energy Environ. Sci.*, 2012, **5**, 5577–5591.

13 B. Hinnemann, P. G. Moses, J. Bonde, K. P. Jørgensen, J. H. Nielsen, S. Horch, I. Chorkendorff and J. K. Nørskov, *J. Am. Chem. Soc.*, 2005, **127**, 5308–5309.

14 T. F. Jaramillo, K. P. Jørgensen, J. Bonde, J. H. Nielsen, S. Horch and I. Chorkendorff, *Science*, 2007, **317**, 100–102.

15 M. V. Bollinger, J. V. Lauritsen, K. W. Jacobsen, J. K. Nørskov, S. Helveg and F. Besenbacher, *Phys. Rev. Lett.*, 2001, **87**, 196803.

16 D. Merki and X. Hu, *Energy Environ. Sci.*, 2011, **4**, 3878–3888.

17 M.-R. Gao, Y.-F. Xu, J. Jiang, Y.-R. Zheng and S.-H. Yu, *J. Am. Chem. Soc.*, 2012, **134**, 2930–2933.

18 W. Zhou, X.-J. Wu, X. Cao, X. Huang, C. Tan, J. Tian, H. Liu, J. Wang and H. Zhang, *Energy Environ. Sci.*, 2013, **6**, 2921–2924.

19 Z. Chen, D. Cummins, B. N. Reinecke, E. Clark, M. K. Sunkara and T. F. Jaramillo, *Nano Lett.*, 2011, **11**, 4168–4175.

20 X. Huang, Z. Zeng, S. Bao, M. Wang, X. Qi, Z. Fan and H. Zhang, *Nat. Commun.*, 2013, **4**, 1444.

21 J. R. McKone, E. L. Warren, M. J. Bierman, S. W. Boettcher, B. S. Brunschwig, N. S. Lewis and H. B. Gray, *Energy Environ. Sci.*, 2011, **4**, 3573–3583.

22 Y. Li, H. Wang, L. Xie, Y. Liang, G. Hong and H. Dai, *J. Am. Chem. Soc.*, 2011, **133**, 7296–7299.

23 Y.-H. Chang, C.-T. Lin, T.-Y. Chen, C.-L. Hsu, Y.-H. Lee, W. Zhang, K.-H. Wei and L.-J. Li, *Adv. Mater.*, 2013, **25**, 756–760.

24 L. Qu, Y. Liu, J.-B. Baek and L. Dai, *ACS Nano*, 2010, **4**, 1321–1326.

25 Z. Yang, Z. Yao, G. Li, G. Fang, H. Nie, Z. Liu, X. Zhou, X. A. Chen and S. Huang, *ACS Nano*, 2011, **6**, 205–211.

26 L. Yang, S. Jiang, Y. Zhao, L. Zhu, S. Chen, X. Wang, Q. Wu, J. Ma, Y. Ma and Z. Hu, *Angew. Chem., Int. Ed.*, 2011, **50**, 7132–7135.

27 Z.-W. Liu, F. Peng, H.-J. Wang, H. Yu, W.-X. Zheng and J. Yang, *Angew. Chem., Int. Ed.*, 2011, **50**, 3257–3261.

28 R. J. Toh, H. L. Poh, Z. Sofer and M. Pumera, *Chem.–Asian J.*, 2013, **8**, 1295–1300.

29 V. Petrykin, K. Macounova, O. A. Shlyakhtin and P. Krtil, *Angew. Chem., Int. Ed.*, 2010, **49**, 4813–4815.

30 K. Fujimura, A. Seko, Y. Koyama, A. Kuwabara, I. Kishida, K. Shitara, C. A. J. Fisher, H. Moriwake and I. Tanaka, *Adv. Energy Mater.*, 2013, **3**, 980–985.

31 G. Kresse and J. Hafner, *Phys. Rev. B: Condens. Matter Mater. Phys.*, 1993, **48**, 13115–13118.

32 G. Kresse and J. Furthmüller, *Comput. Mater. Sci.*, 1996, **6**, 15–50.

33 P. E. Blöchl, *Phys. Rev. B: Condens. Matter Mater. Phys.*, 1994, **50**, 17953–17979.

34 G. Kresse and D. Joubert, *Phys. Rev. B: Condens. Matter Mater. Phys.*, 1999, **59**, 1758–1775.

35 J. P. Perdew, K. Burke and M. Ernzerhof, *Phys. Rev. Lett.*, 1996, **77**, 3865–3868.

36 Z. B. Z. Wei, P. Grange and B. Delmon, *Appl. Surf. Sci.*, 1998, **135**, 107–114.

37 W. Zhou, Z. Yin, Y. Du, X. Huang, Z. Zeng, Z. Fan, H. Liu, J. Wang and H. Zhang, *Small*, 2013, **9**, 140–147.

38 J. Liu, S. Tang, Y. Lu, G. Cai, S. Liang, W. Wang and X. Chen, *Energy Environ. Sci.*, 2013, **6**, 2691–2697.

39 Q. Xiang, J. Yu, W. Wang and M. Jaroniec, *Chem. Commun.*, 2011, **47**, 6906–6908.

40 S. Wang, J. Xu, H. Ding, S. Pan, Y. Zhang and G. Li, *CrystEngComm*, 2012, **14**, 7672–7679.

41 J. G. N. Thomas, *Trans. Faraday Soc.*, 1961, **57**, 1603–1611.

42 J. Xie, H. Zhang, S. Li, R. Wang, X. Sun, M. Zhou, J. Zhou, X. W. Lou and Y. Xie, *Adv. Mater.*, 2013, **25**, 5807–5813.